PAPER

Check for updates

Ultrafast acoustic vibrations of Au–Ag nanoparticles with varying elongated structures†

Xin Zhao,[a] Zhaogang Nie, ID *[ab] Yuhua Feng,[c] Weiren Zhao,[a] Jiahua Zhang, ID [d] Wenchun Zhang,[e] Paolo Maioli ID *[f] and Zhi-Heng Loh[b]

Acoustic vibrations of Au and Ag elongated nano-objects with original morphologies, from Ag–Ag homodimers to Au@Ag–Ag heterodimers and Au@Ag eccentric core–shell spheroids, have been experimentally investigated by ultrafast time-resolved optical spectroscopy. Their frequencies, obtained by the analysis of time-dependent transient absorption changes, are compared with the results obtained from finite element modeling (FEM) numerical computations, which allow assignment of the detected oscillating signals to fundamental radial and extensional modes. FEM was further used to analyze the effects of morphology and composition on the vibrational dynamics. FEM computations indicate that (1) the central distance between particles forming the nanodimers has profound effects on the extensional mode frequencies and a negligible influence on the radial mode ones, in analogy with the case of monometallic nanorods, (2) coating Au with Ag also has a strong mass-loading-like effect on the dimer and core–shell stretching mode frequency, while (3) its influence on the radial breathing mode is smaller and analogous to the non-monotonic frequency dependence on the Au fraction previously observed in isotropic bimetallic spheres. These findings are significant for developing a predictive understanding of nanostructure mechanical properties and for designing new mechanical nanoresonators.

Introduction

Over the past few decades, noble-metal nanoparticles have received increasing attention due to their original optical and mechanical properties.[1–5] The most intriguing one is represented by their localized surface plasmon resonance (SPR), whose characteristics are sensitive to size, shape, environment and composition.[1–7] The optical absorption and scattering enhancement induced by the SPR allows investigation of their vibrational dynamics by detecting their time-resolved optical response with ultrafast laser techniques.[3,8,9] Information obtained by the study of the vibrational dynamics is of both fundamental

and technological interest. For example, it allows addressing the influence of particle size, morphology, interface conditions and mutual mechanical contacts on the nanostructure vibrations,[8] to characterize the coupling with the surrounding environment,[9–12] and to design ultrasensitive mechanical nanobalances that detect a frequency shift of vibrational modes when a small mass deposits on the particle surface.[13–16]

Currently, there is rapidly growing interest in Au–Ag bimetallic nano-objects since they present not only a combination of properties associated with monometallic Au or Ag, but also novel performances due to their synergistic effects.[17–20] However, their acoustic signatures have been little investigated in experiments.[21–25] So far, some Au–Ag bimetallic nanosystems, such as alloyed spheres,[21,23,25] nanoboxes and nanocages,[22] and segregated spheres,[25] nanorods[24] and bipyramids,[16] were studied by Raman spectroscopy and time-resolved pump–probe experiments. Other experimental reports focused on concentric spherical and rod-shaped hetero-structures with Au or Ag as the core, but with other metals or dielectrics as the shell.[25–29] All these results show excellent mechanical coupling of bimetallic components and an increasing quantitative understanding of their interactions.

Here, we report on the coherent excitation and detection of vibrational modes in Au–Ag composite nano-objects using femtosecond time-resolved pump–probe spectroscopy. The object structures (see Fig. 1) are varied from Ag–Ag homodimers

a School of Physics and Optoelectronic Engineering, Guangdong University of Technology, Guangzhou 510006, Guangdong, China. E-mail: zgnie@gdut.edu.cn

b Division of Chemistry and Biological Chemistry, School of Physical and Mathematical Sciences, Nanyang Technological University, 21 Nanyang Link, Singapore 637371, Singapore

c Institute of Advanced Synthesis, School of Chemistry and Molecular Engineering, Nanjing Tech University, Nanjing 211816, Jiangsu, China

d State Key Laboratory of Luminescence and Applications, Changchun Institute of Optics, Fine Mechanics and Physics, Chinese Academy of Sciences, Changchun 130033, China

e College of Traditional Chinese Medicine, Jiangxi University of Traditional Chinese Medicine, Nanchang 33004, China

f University of Lyon, Université Claude Bernard Lyon 1, CNRS, Institut Lumière Matière, Villeurbanne, F-69622, France. E-mail: paolo.maioli@univ-lyon1.fr

† Electronic supplementary information (ESI) available. See DOI: 10.1039/d0cp03260c
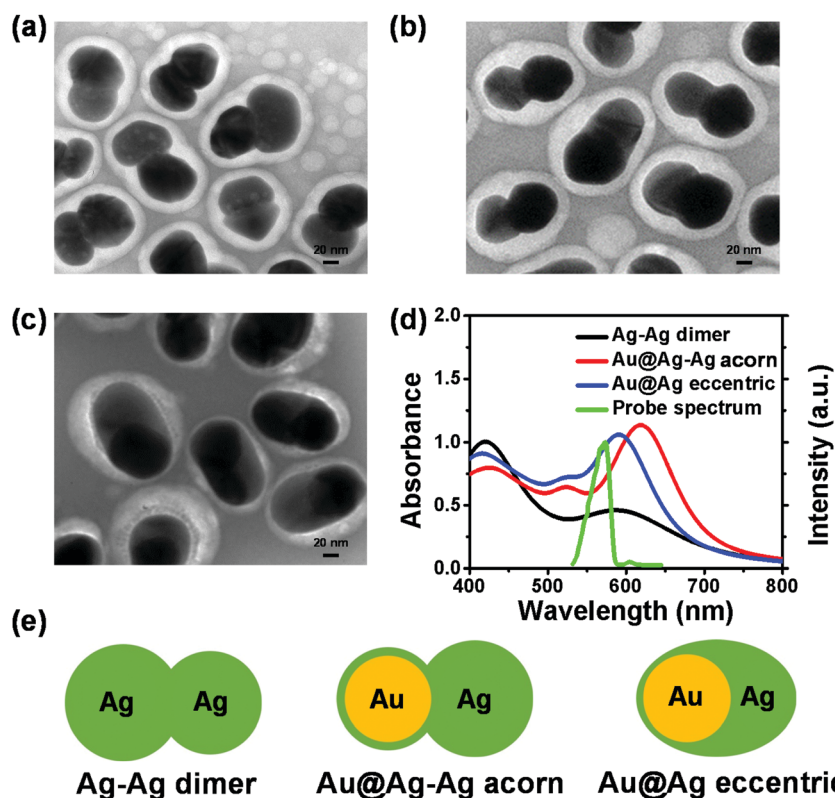
Fig. 1 TEM images of (a) Ag–Ag dimers, (b) Au@Ag–Ag acorn-shaped heterodimers, and (c) Au@Ag core–shell eccentric spheroids (all shapes are illustrated in panel (e)), and (d) their linear absorption spectra. The laser probe spectrum (540–590 nm range, on the blue side of the strongest longitudinal absorption) is indicated by a green line.

to more singular bimetallic morphologies such as Au@Ag–Ag acorn-shaped heterodimers, made of an Au core–Ag shell Au@Ag sphere and a second monometallic larger Ag sphere, and Au@Ag eccentric core–shell spheroids, made of an eccentric Au core embedded in an Ag shell. Two vibrational modes are systematically detected, attributed to vibrations along radial and axial directions. Finite element modeling (FEM) analysis supports the vibrational mode assignments and permits us to finely analyze the influence of particle morphology and composition on the acoustic response of elongated nanoparticles.

Methods

Sample synthesis and characterization

The samples were chemically synthesized using a seed-mediated growth technique in aqueous solution,[20] described in detail in Section 1 of the ESI.† Citrate-stabilized Au or Ag nanoparticles with 2-mercaptobenzimidazole-5-carboxylic acid (MBIA) ligands were used as seeds for growing Ag. By varying ligand conditions (MBIA concentration and incubation temperature) during the growth of Ag on Au or Ag seeds, the morphology of composite nanoparticles can be continuously tuned from concentric to eccentric core–shell nanoparticles, acorn-like shapes and dimers.[20] This allowed the synthesis of three samples containing nanoparticles with different structures (Fig. 1e): (1) Ag–Ag homo-dimers, (2) Au@Ag–Ag acorn-shaped heterodimers (also referred

to as acorns) and (3) Au@Ag eccentric core–shell prolate spheroids (i.e. ellipsoids with two equal minor axes). Analysis of transmission electron microscopy (TEM) images (Fig. 1a–c) indicates mean particle sizes in the 50–100 nm range with standard deviations around ∼10 nm. The morphological parameters are listed in Table 1.

For the synthesis of the Ag–Ag dimers (sample 1), Au@Ag concentric core–shell nanoparticles with ∼65 nm external diameter were firstly synthesized following a literature report.[30] The small Au core, with a diameter varying from 10 to 15 nm, was necessary to grow large Ag spheres with low size dispersion. The Au@Ag nanoparticles were subsequently used as seeds for growing a second Ag sphere, resulting in the formation of dimers (Fig. 1a). As discussed later, the impact of the small Au core (corresponding to a volume equivalent to less than 1% of the

Table 1 Sizes of Ag–Ag dimers, Au@Ag–Ag acorn-shaped dimers and Au@Ag eccentric core–shell nanospheroids. The Au@Ag core–shell sphere forming Au@Ag–Ag acorns is made of a 51 nm diameter inner Au sphere surrounded by a 5 nm thick Ag shell. The 65 nm seed Ag sphere in Ag–Ag dimers contains an inner Au core with a diameter of around 10–15 nm

Sample	Diameter (nm)	Diameter (nm)	Total length (nm)
Ag–Ag dimers	65 ± 7 (Ag)	63 ± 10 (Ag)	102 ± 10
Au@Ag–Ag acorns	61 ± 7 (Au@Ag)	69 ± 10 (Ag)	113 ± 14
Au@Ag spheroids	58 ± 7 (Au)	80 ± 8 (Ag)	110 ± 12

This journal is © the Owner Societies 2020

Phys. Chem. Chem. Phys., 2020, 22, 22728–22735 | 22729

volume of the sphere) on the periods of the lowest-frequency vibrational modes, which are the main focus of this work, is insignificant. Thus, for simplicity, these dimers will be simply referred to as monometallic Ag–Ag dimers in the following. For synthesizing Au@Ag–Ag acorn-shaped dimers (sample 2) and eccentric core–shell nanospheroids (sample 3), citrate-stabilized pure Au nanoparticles, synthesized by a citrate-reduction method, were used as seeds. The thickness of the Ag shell embedding the Au nanospheres in Au@Ag–Ag acorns and the one of the thinnest Ag shells in Au@Ag eccentric core–shell nanoparticles is around 5 nm.

Steady-state absorption spectra of nanoparticles in water are shown in Fig. 1d. Three absorption bands are distinguishable: longitudinal SPR, centered around 600 to 650 nm,[20] Ag transverse plasmon-induced absorption around 425 nm and weak Au transverse plasmon-induced absorption around 510 nm (superposed to Au interband absorption[31] and absent in the Ag–Ag dimer sample).

Prior to deposition on carbon TEM grids, to avoid aggregation and better distinguish their boundaries, nanoparticles were encapsulated with a ~12 nm thin polymer shell of PSPAA (polystyrene-*block*-poly(acrylic acid), white layer around the dark metal particles in Fig. 1a–c). The Au seeds and the Ag islands grown on the seeds are all polycrystalline. The purity of the synthesized nanoparticles was very high (~98% out of ~500 nanoparticles surveyed). Azide-functionalized Au nano-rods with similar dimensions were also prepared and used as a reference for time-resolved optical experiments and their analysis (ESI,† Section 5).

Time-resolved optical spectroscopy

Vibrational dynamics of nanoparticles in water was investigated by ultrafast time-resolved optical spectroscopy. Broadband femtosecond pump pulses, with a fluence of around 0.1 mJ cm^{-2} and covering the spectral range from ~500 to 900 nm, were used for impulsive excitation, the sample optical response being followed by monitoring the relative variations $\Delta T/T$ of the optical transmission of a time-delayed probe pulse with wavelengths tunable from 540 to 590 nm (on the blue side of the strongest absorption band, see Fig. 1d, refer to Section 2 of the ESI† for details of the optical setup). Pump and probe beams are orthogonally polarized to minimize the effects from coherent artifacts. A time resolution of ~52 fs fwhm for the apparatus was revealed by a second-order intensity cross-correlation between pump and probe pulses (see Fig. S1c, ESI†). For time-resolved measurements, nanoparticle solutions (with no polymer) were contained in 1 mm thick fused-silica cuvettes.

Results and discussion

Time-resolved detection of mechanical vibrational modes

Time-resolved relative transmission changes $\Delta T/T$ for Ag–Ag dimers, Au@Ag–Ag acorns and Au@Ag eccentric core–shell spheroids are portrayed in Fig. 2a–c and Fig. S2a–c (ESI†). After electron excitation by absorption of the pump pulse and

internal thermalization, energy is transferred from electrons to the lattice by electron–phonon interactions, within a time-scale of a few picoseconds. The fast lattice temperature increase launches nanoparticle mechanical acoustic vibrations, which translate into periodic oscillations of time-resolved optical transmission (black lines in Fig. 2a–c), induced by the spectral modulation of central SPR positions.[3,8,31–33] As expected, oscillations are all in-phase (see Fig. S2d–f, ESI†), as probe wavelengths all lie on the same side of longitudinal and transverse absorption bands.[34] Note that a different choice of probe wavelengths may results in signals oscillating with different amplitudes and opposite phases but the same frequencies, as the latter reflects the ones of mechanical acoustic vibrations.

The decreasing parts of the signals can be accurately reproduced by a sum of two decaying exponentials, with time constants τ_{e-p} and τ_{th}, respectively, associated with electron to lattice energy transfer by electron–phonon coupling and lattice to environment thermal energy exchange, and two damped cosine functions associated with lattice vibrations of period T_v, leading to the following fit function:

$$S(t) = A_{e-p}e^{-t/\tau_{e-p}} + A_{th}e^{-t/\tau_{th}}$$
$$+ \sum_{v=1,2} A_v e^{-t/\tau_v} \cos(2\pi t/T_v + \varphi_v) \quad (1)$$

where A_{e-p} and A_{th} describe the amplitudes of the decaying exponentials and A_v, τ_v, T_v and φ_v are the amplitude, damping time, period and phase, respectively, of the acoustic oscillations. The fast electron cooling dynamics *via* electron–phonon coupling has a characteristic time of a few picoseconds,[35] while the slow thermal dissipation to the surrounding water matrix shows a typical timescale longer than 100 ps. The values of vibrational periods deduced by fits (red lines in Fig. 2a–c, the two oscillating components of the fits being shown in the insets), which are the main focus of this work, are reported in Table 2. Fourier transform (FT) of the oscillating contributions to the $\Delta T/T$ signals (after subtraction of the decaying exponentials) is shown in Fig. 2d–f. For all the samples, the two frequencies obtained correspond to the periods (T_1 and T_2) deduced by the fits in the time domain. The shorter period for all the samples is around 20 ps (~50 GHz), longer than the time constant (τ_{e-p}) of the electron to lattice energy transfer, of a few ps, responsible for impulsive vibration launching.[3,8]

Frequency analysis by comparison with FEM

To clarify the identity of the vibrational modes, FEM computations were performed introducing the sample sizes deduced by TEM images and simulating elastic response using polycrystalline elastic constants for gold and silver[36] (also see the ESI,† Section 4). FEM was used to (1) numerically compute the vibrational eigenmodes corresponding to each specific sample morphology and (2) identify the ones which are most excited in time-resolved optical experiments, *i.e.* those whose atom displacements best match the uniform spatial dilation induced by the pump excitation.[8,37] Note that FEM computations are made for objects in a vacuum, which is justified as vibrational

22730 | *Phys. Chem. Chem. Phys.*, 2020, **22**, 22728–22735

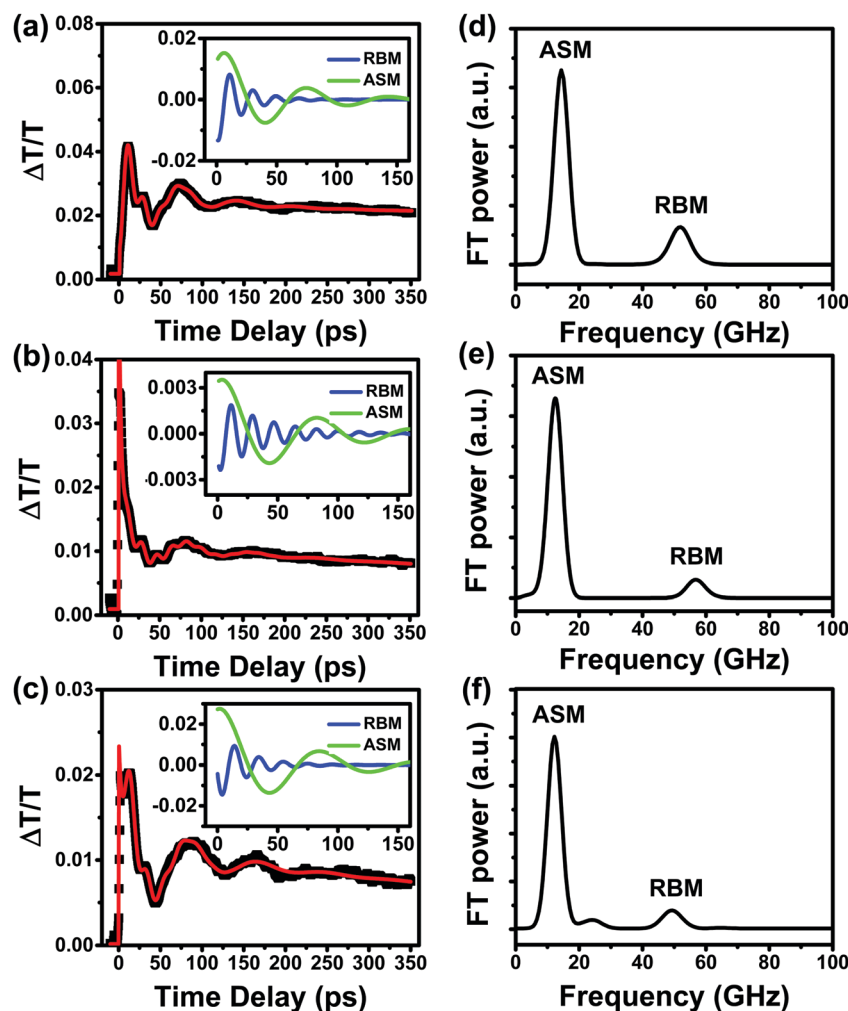This journal is © the Owner Societies 2020

Fig. 2 Time-resolved differential transmission changes $\Delta T/T$ (black lines) measured with a 570 nm probe wavelength, for (a) Ag–Ag dimers, (b) Au@Ag–Ag acorn-shaped heterodimers, and (c) Au@Ag core–shell eccentric spheroids, and their fits (red lines) by a sum of two exponential and two damped cosine functions (eqn (1)) convoluted with the system response function. Inset: Two damped vibrational contributions (RBM and ASM) to the fits (blue and green lines) due to the main RBM and ASM, respectively. (d–f) Fourier transforms of $\Delta T/T$ time-resolved signals after subtraction of the exponential components.

Table 2 Vibrational periods (T_1 and T_2) deduced by the fits of time-resolved transient absorption signals on the three metallic samples

Samples	T_1 (ps)	T_2 (ps)
Ag–Ag dimers	19.7 ± 1.2	69 ± 3
Au@Ag–Ag acorns	17.7 ± 1.0	84 ± 5
Au@Ag spheroids	21.0 ± 2.0	82 ± 3

periods are almost unchanged when in a liquid environment (period decrease by $\sim 0.2\%$ in the case of spherical nanoparticles) compared to vacuum.[38] The rationality of FEM is also verified by supplementary time-resolved investigations on Au nanorods with consistent experimental and theoretical results (see the ESI,† Section 5).

Ag–Ag dimers. Fig. 3a displays the FEM-computed displacement profiles of the most excited vibrational modes of Ag–Ag dimers, corresponding to a fundamental axial stretching-like mode (ASM, Fig. 3a, left) and radial breathing-like mode (RBM,

right). As already mentioned, all FEM computations on the Ag–Ag dimer morphology have been made considering an Ag monometallic dimer, *i.e.* disregarding the small Au core at the center of the 65 nm Ag sphere used as a seed for growing the second Ag sphere. This is justified as the expected change of the dimer ASM and RBM frequencies due to inclusion of the small Au core ($<1\%$ Au atomic fraction), compared to the case of a monometallic Ag sphere, is negligible (within numerical precision), as preliminarily benchmarked and also in analogy with the case of the breathing mode of Au@Ag spheres previously reported (the influence of this internal structuration is expected to be much larger for higher frequency vibrational modes).[25] The detected mode with the longer period (T_2, red square in Fig. 4a) is assigned to dimer ASM (Fig. 4a, open diamond corresponding to the same horizontal position), the one with the shorter period (T_1, black dot) is attributed to dimer RBM (open triangle). The dimer RBM displacement profile (Fig. 3a, right) is similar to the one of the in-phase fundamental
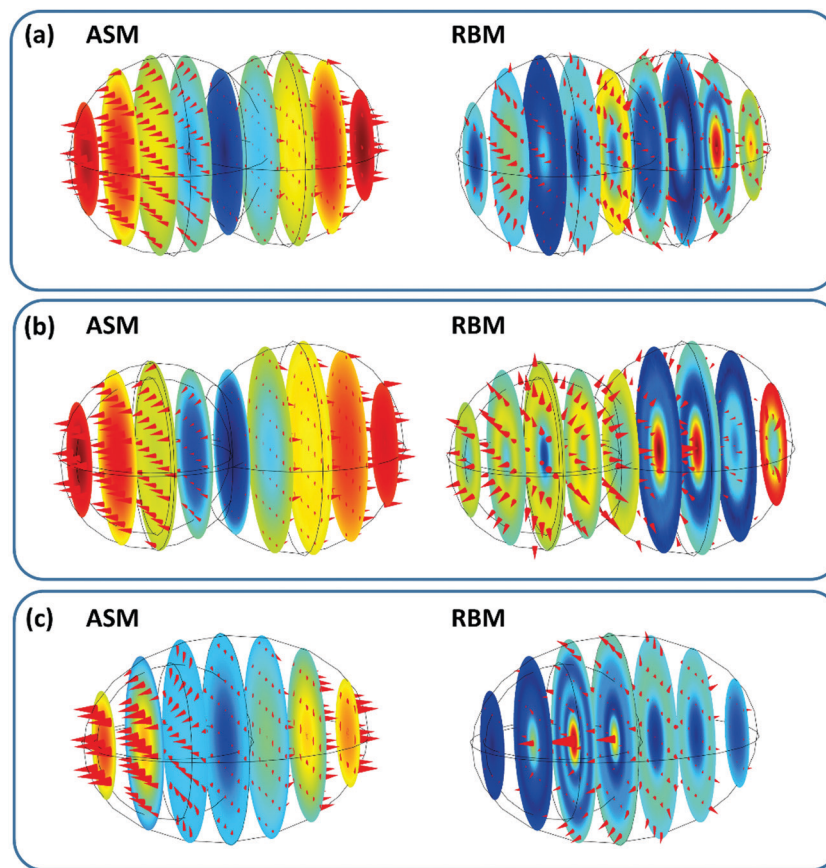
Fig. 3 FEM computed displacement profiles of the most excited modes, the axial stretching-like mode (ASM, left) and the radial breathing-like mode (RBM, right), for (a) Ag–Ag dimers, (b) Au@Ag–Ag acorn-shaped heterodimers, and (c) Au@Ag core–shell eccentric spheroids. Arrows and colors represent directions and amplitudes (increasing from blue to red) of the displacement vectors.

radial breathing mode of the two isolated Ag spheres (see Fig. S4, ESI†), whose period (black cross in Fig. 4a, corresponding to the breathing mode of an isolated Ag sphere with the diameter of the larger sphere composing the Ag–Ag dimer) is close to the one numerically computed for the dimer RBM (open triangle). Dimer RBM period is thus approximately independent of the dimer length (Fig. 4a, open triangles, computed for three different dimer lengths, corresponding to different center-to-center distances of the two spheres composing the dimer). Conversely, the dimer ASM displacement profile (Fig. 3a, left) is induced by the anisotropic quadrupolar-mode-like vibrations of the spherical components (whose displacements consist of periodical particle expansion and contractions along one direction with synchronous out-of-phase deformation in the perpendicular plane, see Fig. S4, ESI†) and its computed period increases with the length of the dimer (Fig. 4a, open diamonds), in analogy with the case of the extensional mode of monometallic nanorods.[37,39] Note that individual quadrupolar modes of the two spheres forming the Ag–Ag dimers, predicted at ∼45 ps (Fig. S4, ESI†), are not detected, in agreement with previous investigations on single Au–Au dimers.[40] Agreement of FEM-computed Ag–Ag dimer RBM and ASM periods (Fig. 4a, open triangle and diamond) with experimental values (solid dot and square) is good, and limited mainly by the relatively large size dispersion of the sample

morphologies, used as input parameters for FEM computations, and by the choice of the polycrystalline Ag elastic constants (different sets of elastic constants predicting slightly different frequencies).[41] In addition, even though they are polycrystalline, nanodimers are composed of very few grains,[20] thus their elastic response (particularly the frequencies of radially anisotropic axial stretching modes, which are more dependent on crystallinity[3,37]) may deviate from that of purely polycrystalline nano-objects.

Au@Ag–Ag acorn-shaped heterodimers. In the case of acorn-shaped bimetallic dimers, FEM computations (Fig. 3b) predict an ASM period depending sensitively on the composition (Fig. 4b, open diamonds). When the smaller 61 nm diameter core–shell Au@Ag sphere (with Au core diameter of 51 nm and Ag shell thickness of 5 nm, corresponding to ∼58% Au fraction) is replaced by a monometallic Ag (Au) sphere indeed, the dimer ASM period is expected to decrease (increase) significantly (Fig. 4b, open diamonds, the horizontal axis indicates the varying composition). This behavior suggests a mass-loading-like effect on the ASM dynamics, the metal with a larger density ($\rho_{Au} = 19\,284$ kg m^{-3} larger than $\rho_{Ag} = 10\,501$ kg m^{-3}) inducing slower extensional vibrations, in analogy to previous computations on Au nanorods with Pd deposited on their tips.[27] Due to the larger difference (compared to Ag–Ag dimers) between the diameters of the two spheres composing the acorn-shaped
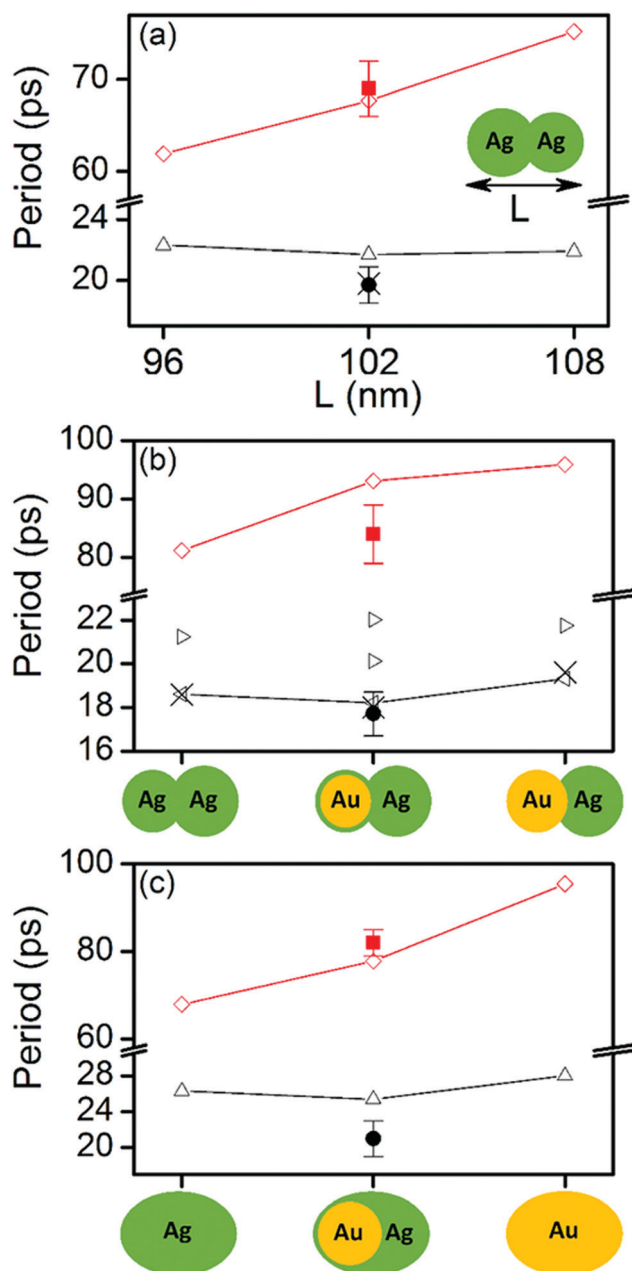
Fig. 4 Experimentally detected RBM (black dots) and ASM (red squares) periods for (a) Ag–Ag dimers, (b) Au@Ag–Ag acorn-shaped heterodimers, and (c) Au@Ag core–shell eccentric spheroids and FEM-computed periods (open triangles and diamonds for RBM and ASM respectively). (a) Horizontal axis represents the total length of the dimer. The black cross indicates the computed breathing mode period of an isolated 65 nm diameter Ag sphere. (b) The three horizontal positions correspond to the three different dimer compositions considered: monometallic Ag–Ag, Au@Ag–Ag (corresponding to the experimental sample) and Au–Ag. Open triangles pointing to the right (left) indicate computed periods of the dimer RBM corresponding to radial breathing-like displacement profiles of the larger Ag sphere (of the smaller sphere with varying composition). Black crosses show the expected breathing mode periods of an isolated Ag, Au@Ag and Au (from left to right) 61 nm diameter sphere. (c) The three horizontal positions correspond to Ag, Au@Ag eccentric core–shell (corresponding to the experimental sample) and Au spheroids with the same external dimensions.

heterodimers, different RBM vibrational modes are expected to be observable in time-resolved experiments, whose displacement profiles contain mixed contributions from both spheres but essentially correspond to mechanical breathing of the core–shell (periods indicated as left-pointing open triangles in Fig. 4b, corresponding to the displacement profile presented in Fig. 3b) and of the larger Ag sphere (Fig. 4b, right-pointing triangles, two dimer modes with breathing-like displacements of the larger Ag spheres being identified in the case of the Au@Ag–Ag composition), all in qualitative agreement with the detected shorter period (black dot). Note that, due to the significant particle-to-particle size and shape dispersion, coherent effects such as beating of oscillations induced by different predicted RBMs are not observed. The dependence of the dimer RBM period corresponding to the mechanical breathing of the core–shell sphere on its composition (left-pointing open triangles in Fig. 4b) is small and non-monotonic: starting from the pure Ag–Ag dimer and replacing the Ag sphere first by a core–shell Au@Ag sphere (corresponding to the experimental sample) and then by a monometallic Au sphere induces a reduction and a subsequent increase of predicted RBM periods. Interestingly, this behavior is in agreement with the trend of the breathing mode period of isolated bimetallic spheres, as shown both by FEM computations (Fig. 4b, crosses) and also previously analytically predicted (through solution of the Navier equation with continuous boundary conditions for displacement and stress at the core–shell interface) and experimentally demonstrated.[25] The predicted ASM period is 15% larger than the one observed. This discrepancy can again be attributed to the large error bars in the determination of the nanodimer morphology, *i.e.* in the deduction of the total length and, more importantly, of the Ag shell thickness, as considering an Ag shell thickness larger than 5 nm would induce a fast reduction of the expected ASM period (Fig. 4b). Time-resolved experiments on single nano-objects (with parallel morphology determination by electron microscopy imaging) may lead to a better agreement with the predicted ASM period.[12,40]

Au@Ag eccentric core–shell nanoparticles. Analogously, FEM-computed ASM periods of bimetallic Au and Ag nanospheroids (Fig. 4c, open diamonds) manifest a strong increase (~30%) when replacing Ag with Au, the ASM period of the Au@Ag eccentric core–shell spheroid (corresponding to the experimentally investigated sample, computed displacement profile shown in Fig. 3c) being intermediate. This dependence may also be viewed as a mass-loading-like effect, inclusion of the material with a larger density slowing down the extensional motion. Again, the corresponding RBM periods (Fig. 4c, open triangles) show the non-monotonic dependence on composition theoretically and experimentally reported for bimetallic spheres, which underlines the analogy between the RBM motion of elongated nanoparticles and breathing mode of isotropic nanospheres. Experimental ASM and RBM periods are again in good agreement with the ones numerically computed. Interestingly, FT of the time-resolved signal on Au@Ag eccentric core–shell nanoparticles allows distinguishing an additional peak (Fig. 2f), with a frequency (~24 GHz) intermediate between those of ASM and

RBM modes. This peak originates from a hybrid mode whose displacement profile (Fig. S5b, ESI†) basically corresponds to the first harmonic of dimer axial stretching, characterized by dimer extension along the long axis with synchronous dilation of the equatorial plane and contraction of the two intermediate orthogonal planes (see also Fig. S5a, ESI,† for the representation of this mode in the simplified case of an homogeneous spheroid).

Conclusions

In conclusion, fundamental RBM and ASM of Au and Ag elongated nano-objects, from monometallic Ag dimers to bimetallic acorn-like shapes and eccentric core–shell spheroids, were coherently excited and probed by femtosecond time-resolved optical spectroscopy. Analysis of transient absorption signals yields acoustic vibrational frequencies whose assignment to specific vibrational modes was accomplished *via* FEM numerical computations, which were further used to analyze the effects of particle morphology and composition on the vibrational dynamics. The axial extensional periods increase with the length of the elongated structures, and with the inclusion of Au at the place of Ag, highlighting a mass-loading-like effect. The RBM mode shows a negligible frequency dependence on the nano-object length, while its dependence on the constituting metals shows a non-monotonic trend, previously observed in isotropic bimetallic Au@Ag spheres. These findings may contribute to the understanding of mutual interactions in bimaterial nano-objetcs and to the development of mechanical applications of Au–Ag bimetallic nanostructures such as mechanical nanotransducers.

Conflicts of interest

There are no conflicts to declare.

Acknowledgements

References

1 V. Myroshnychenko, J. Rodríguez-Fernández, I. Pastoriza-Santos, A. M. Funston, C. Novo, P. Mulvaney, L. M. Liz-Marzán and F. J. García de Abajo, *Chem. Soc. Rev.*, 2008, **37**, 1792–1805.

2 P. K. Jain, X. Huang, I. H. El-Sayed and M. A. El-Sayed, *Plasmonics*, 2007, **2**, 107–118.

3 G. V. Hartland, *Chem. Rev.*, 2011, **111**, 3858–3887.

4 A. Crut, P. Maioli, N. Del Fatti and F. Vallée, *Chem. Soc. Rev.*, 2014, **43**, 3921–3956.

5 V. Amendola, R. Pilot, M. Frasconi, O. M. Maragò and M. Antonia Iatì, *J. Phys.: Condens. Matter*, 2017, **29**(20), 203002.

6 A. Crut, P. Maioli, F. Vallée and N. Del Fatti, *J. Phys.: Condens. Matter*, 2017, **29**(12), 123002.

7 E. Pertreux, A. Lombardi, I. Florea, M. Spuch-Calvar, S. Gómez-Graña, D. Ihiawakrim, C. Hirlimann, O. Ersen, J. Majimel, M. Tréguer-Delapierre, M. Hettich, P. Maioli, A. Crut, F. Vallée and N. Del Fatti, *Adv. Opt. Mater.*, 2016, **4**(4), 567–577.

8 A. Crut, P. Maioli, N. Del Fatti and F. Vallée, *Phys. Rep.*, 2015, **549**, 1–43.

9 M. Pelton, J. E. Sader, J. Burgin, M. Liu, P. Guyot-Sionnest and D. Gosztola, *Nat. Nanotechnol.*, 2009, **4**, 492–495.

10 R. Marty, A. Arbouet, C. Girard, A. Mlayah, V. Paillard, V. K. Lin, S. L. Teo and S. Tripathy, *Nano Lett.*, 2011, **11**, 3301–3306.

11 T. A. Major, A. Crut, B. Gao, S. S. Lo, N. Del Fatti, F. Vallée and G. V. Hartland, *Phys. Chem. Chem. Phys.*, 2013, **15**, 4169–4176.

12 F. Medeghini, A. Crut, M. Gandolfi, F. Rossella, P. Maioli, F. Vallée, F. Banfi and N. Del Fatti, *Nano Lett.*, 2018, **18**(8), 5159–5166.

13 Y. T. Yang, C. Callegari, X. L. Feng, K. L. Ekinci and M. L. Roukes, *Nano Lett.*, 2006, **6**, 583–586.

14 J. Chaste, A. Eichler, J. Moser, G. Ceballos, R. Rurali and A. Bachtold, *Nat. Nanotechnol.*, 2012, **7**, 301–304.

15 G. Benetti, M. Gandolfi, M. J. Van Bael, L. Gavioli, C. Giannetti, C. Caddeo and F. Banfi, *ACS Appl. Mater. Interfaces*, 2018, **10**, 27947–27954.

16 A. D. Fernandes, M. Spuch-Calvar, H. Baida, M. Tréguer-Delapierre, J. Oberle, P. Langot and J. Burgin, *ACS Nano*, 2013, **7**, 7630–7639.

17 Z. D. Hood, K. P. Kubelick, K. D. Gilroy, D. Vanderlaan, X. Yang, M. Yang, M. Chi, S. Y. Emelianov and Y. Xia, *Nanoscale*, 2019, **11**, 3013–3020.

18 Z. Huang, G. Meng, X. Hu, Q. Pan, D. Huo, H. Zhou, Y. Ke and N. Wu, *Nano Res.*, 2019, **12**, 449–455.

19 E. E. Elemike, D. C. Onwudiwe, O. E. Fayemi and T. L. Botha, *Appl. Phys. A*, 2019, **125**, 4.

20 Y. Feng, J. He, H. Wang, Y. Y. Tay, H. Sun, L. Zhu and H. Chen, *J. Am. Chem. Soc.*, 2012, **134**, 2004–2007.

21 H. Portales, L. Saviot, E. Duval, M. Gaudry, E. Cottancin, J. Lermé, M. Pellarin, M. Broyer, B. Prével and M. Treilleux, *Eur. Phys. J. D*, 2001, **16**, 197–200.

22 H. Petrova, C. H. Lin, M. Hu, J. Chen, A. R. Siekkinen, Y. Xia, J. E. Sader and G. V. Hartland, *Nano Lett.*, 2007, **7**, 1059–1063.

23 S. Adichtchev, S. Sirotkin, G. Bachelier, L. Saviot, S. Etienne, B. Stephanidis, E. Duval and A. Mermet, *Phys. Rev. B: Condens. Matter Mater. Phys.*, 2009, **79**, 201402.

24 L. Wang, A. Kiya, Y. Okuno, Y. Niidome and N. Tamai, *J. Chem. Phys.*, 2011, **134**, 054501.

22734 | *Phys. Chem. Chem. Phys.*, 2020, **22**, 22728–22735

This journal is © the Owner Societies 2020

25 T. Stoll, P. Maioli, A. Crut, J. Burgin, P. Langot, M. Pellarin, A. Sánchez-Iglesias, B. Rodríguez-González, L. M. Liz-Marzán, N. Del Fatti and F. Vallée, *J. Phys. Chem. C*, 2015, **119**, 1591–1599.

26 J. H. Hodak, A. Henglein and G. V. Hartland, *J. Phys. Chem. B*, 2000, **104**, 5053–5055.

27 M. F. Cardinal, D. Mongin, A. Crut, P. Maioli, B. Rodríguez-González, J. Pérez-Juste, L. M. Liz-Marzán, N. Del Fatti and F. Vallée, *J. Phys. Chem. Lett.*, 2012, **3**, 613–619.

28 A. Mongin, V. Juvé, P. Maioli, A. Crut, N. Del Fatti, F. Vallée, A. Sánchez-Iglesias, I. Pastoriza-Santos and L. M. Liz-Marzán, *Nano Lett.*, 2011, **11**, 3016–3021.

29 A. S. Kirakosyan and T. V. Shahbazyan, Vibrational Modes of Metal Nanoshells and Bimetallic Core-Shell Nanoparticles, *J. Chem. Phys.*, 2008, **129**, 034708.

30 W. Xie, L. Su, P. Donfack, A. Shen, X. Zhou, M. Sackmann, A. Maternyb and J. Hu, *Chem. Commun.*, 2009, 5263–5265.

31 T. Stoll, P. Maioli, A. Crut, N. Del Fatti and F. Vallée, *Eur. Phys. J. B*, 2014, **87**, 260.

32 A. Voisin, N. Del Fatti, D. Christofilos and F. Vallée, *J. Phys. Chem. B*, 2001, **105**, 2264–2280.

33 P. Maioli, T. Stoll, H. E. Sauceda, I. Valencia, A. Demessence, F. Bertorelle, A. Crut, F. Vallée, I. L. Garzón, G. Cerullo and N. Del Fatti, *Nano Lett.*, 2018, **18**, 6842–6849.

34 N. D. Fatti, C. Voisin, D. Christofilos, F. Vallée and C. Flytzanis, *J. Phys. Chem. A*, 2000, **104**(18), 4321–4326.

35 D. Mongin, P. Maioli, J. Burgin, P. Langot, E. Cottancin, S. D'Addato, B. Canut, M. Treguer, A. Crut, F. Vallée and N. Del Fatti, *J. Phys.: Condens. Matter*, 2019, **31**(8), 084001.

36 H. Ledbetter and S. Kim, Monocrystal Elastic Constants and Derived Properties of the Cubic and the Hexagonal Elements, *Handbook of Elastic Properties of Solids, Liquids, and Gases*, Academic Press, New York, 2001.

37 A. Crut, P. Maioli, N. Del Fatti and F. Vallée, *Phys. Chem. Chem. Phys.*, 2009, **11**, 5882–5888.

38 C. Voisin, N. Del Fatti, D. Christofilos and F. Vallée, *Appl. Surf. Sci.*, 2000, **164**, 131–139.

39 M. Hu, X. Wang, G. V. Hartland, P. Mulvaney, J. P. Juste and J. E. Sader, *J. Am. Chem. Soc.*, 2003, **125**, 14925–14933.

40 A. L. Tchebotareva, M. A. van Dijk, P. V. Ruijgrok, V. Fokkema, M. H. S. Hesselberth, M. Lippitz and M. Orrit, *ChemPhysChem*, 2009, **10**, 111–114.

41 H. E. Sauceda, D. Mongin, P. Maioli, A. Crut, M. Pellarin, N. Del Fatti, F. Vallée and I. L. Garzón, *J. Phys. Chem. C*, 2012, **116**, 25147–25156.